Fluidic Control of Nacelle Inlet Flow in Crosswind

Derek A. Nichols[1], Bojan Vukasinovic[2], and Ari Glezer[3]
Georgia Institute of Technology, Atlanta, GA 30332-0405

Matthew DeFore[4] and Bradley Rafferty[5]
The Boeing Company

Abstract

The inlet flow of an engine nacelle model is investigated experimentally in the presence of cross flow that induces a complex azimuthal separation pattern over the nacelle's inlet windward surface. The evolution of the separation topology and its response to flow control strategies are investigated in a state-of-the-art crosswind wind tunnel. Fluidically-oscillating jets are utilized as the flow control elements at various intensities and locations for a range of inlet mass flow rates and cross flow speed conditions. Based on these investigations, control approaches are devised for optimal suppression of azimuthal separation within each of three characteristic ranges of the inlet mass flow rate. It is shown that the fluidic actuation pattern within each inlet flow segment yields significant broadband reduction of the total pressure distortion, as measured by the circumferential distortion index IDC_{max}. At cross flow speeds of 30 and 35 knots, IDC_{max} is reduced by about 60 and 50%, respectively, at actuation mass flow rates of less than 0.3% of the maximum inlet mass flow rate. The successful implementation of segment-optimized spatial flow control configurations indicates that dynamic, real-time reconfiguration of the fluidic actuation with varying inlet- and cross flow can yield tuned, optimal control of inlet separation.

Nomenclature

C_q	=	$\dot{m}_j/\dot{m}_c$
D	=	inlet throat diameter
f	=	suction blower operating frequency
f_c	=	suction blower operating frequency at choking
IDC	=	circumferential distortion index
IDC_{max}	=	max circumferential distortion index
$\dot{m}$	=	mass flow rate
$\dot{m}_c$	=	mass flow rate at choking
$\dot{m}^*$	=	$\dot{m}/\dot{m}_c$
$\dot{m}_j$	=	mass flow rate jet
p_a	=	atmospheric pressure
p_o	=	total pressure
p_r	=	pressure ratio across actuator
U_o	=	crosswind speed
y	=	distance from wall
θ	=	azimuthal coordinate

[1] Graduate Research Assistant, AIAA Member.
[2] Research Engineer, AIAA Member.
[3] Professor, AIAA Fellow.
[4] Aerodynamics Engineer, Boeing Commercial Aircraft
[5] Aerodynamics Engineer, Boeing Research & Technology, AIAA Member

I. Background

Aircraft engine nacelles encounter a range of disparate operating stages during all phases of flight and taxi. Because the nacelle inlet is normally optimized aerodynamically for cruise, its aerodynamic performance is often reduced for the other operational stages of the flight. Consequently, selecting the aerodynamic design which is best suited for all aspects of the flight is extremely difficult and must take all stages of operation into consideration.

The performance of aircraft engines close to the ground (taxi, takeoff, and landing) can be strongly impacted by the presence of the ground plane and by crosswind that can significantly alter the air intake at the inlet (Trapp et al., 2006). The presence of a crosswind can lead to the formation of a fuselage vortex, inlet flow separation, and, when coupled with ground effect, the formation of a ground vortex that may cause ingestion of debris into the engine (Colehour and Farquhar, 1971, Trapp and Girardi, 2012).

Of particular interest is inlet flow separation that can occur in the presence of a crosswind during low speed movements or during climb at steep angles (Savelyev, et al., 2014, Maji et al., 2016). The formation of a highly unsteady separation bubble on the windward edge can produce streamwise vortices and lead to interactions with the fan blades which can cause blade damage and even compressor stall (Übelacker and Kähler, 2016, Radespiel et al. 2016). Furthermore, the separation bubble decreases the effective cross-sectional area of the inlet and hence the mass flow rate through the engine for a fixed engine pressure ratio (Übelacker et al., 2014). Earlier investigations have also demonstrated that, because of separation hysteresis with varying intake speed, it is especially challenging to force the flow to reattach to the surface (Hall and Hynes, 2006, Colin et al., 2007). Wakelam et al. (2012a, 2012b) conducted low- and high-speed tests on a cylindrical nacelle sector whose inlet was designed to emulate crosswind flow. In this experimental setup, they explored passive boundary layer trips and active vortex-generating jets for mitigation of flow separation at the lip. These authors reported that mitigation of separation within the three-dimensional sector flow led to reduction in total pressure distortion. Finally, Nichols et al. (2019) investigated the topology of the three-dimensional flow and the evolution of complex flow separation over the windward inlet lip of a nacelle in the presence of orthogonal crosswind up to 35 knots. They explored the effectiveness of autonomous-bleed actuation in three control configurations that were based on the topology of the separated base flow at a given inlet mass flow rate and the two crosswind speeds of 30 and 35 knots.

II. Experimental Setup and Flow Diagnostics

The experiments are conducted in a test facility that was designed and assembled for investigations of the physics of nacelle/cross flow interactions and control of their evolution using fluidic actuation. The facility at Georgia Tech comprises two primary components: a model nacelle assembly and a cross flow wind tunnel (Figure 1). The mass flow rate, position, and orientation of the inlet are all variable, as is the tunnel crosswind speed.

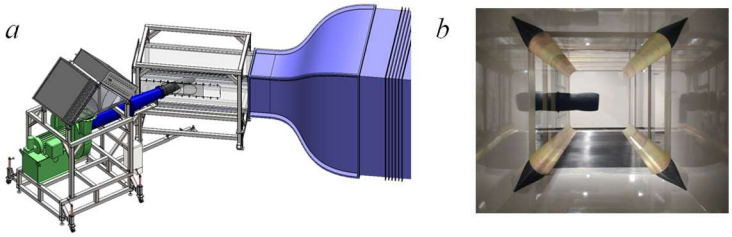

Figure 1*. Test facility (a) and the downstream view of the nacelle model in the wind tunnel test section (b).*

The nacelle model, which can be used to test a broad range of its inlet section configurations, is mounted on a flow duct that is driven in

suction by a computer-controlled blower. The nacelle model, which has a throat inlet diameter D, is attached to a diffuser followed by a long straight duct segment upstream of the blower's inlet. The duct is equipped with a probe for mass flow rate measurements placed between flow straighteners upstream and downstream. The blower exhaust air is driven into the room through two chilled water heat exchangers so that the ambient air temperature in the room is maintained at a prescribed level to within 1°C. The nacelle-duct assembly and the blower are supported on frame that is movable using casters. This frame enables angular and axial adjustability about a pivot at the center of the tunnel test section. The angular adjustment serves to vary crosswind angle with respect to the inlet centerline (side slip). The nacelle height offset is always located midway between the test section floor and ceiling. In the present investigation, the nacelle model is oriented normal to the cross flow direction while protruding halfway into the width of the test section.

The cross flow is generated by an open-return, low-speed wind tunnel having a contraction ratio of 10:1 that is driven by a computer-controlled axial blower. The tunnel's square test section is optically transparent from three sides to enable flow visualization and optical diagnostics of the flow field about the nacelle's inlet. The uniformity of the air speed within the test section was verified using velocity measurements at the test section exit plane in the absence of the nacelle model. The data were acquired over the central nine points of the exit plane, as shown schematically in the inset plot in Figure 2. Each measurement point is characterized over the full range of the cross flow speeds, and the measured velocity distributions are plotted relative to the pressure drop across the tunnel contraction in Figure 2. A rather remarkable collapse of all the measured distributions points to uniform bulk flow in the test section, which can be attained in excess of 50 knots.

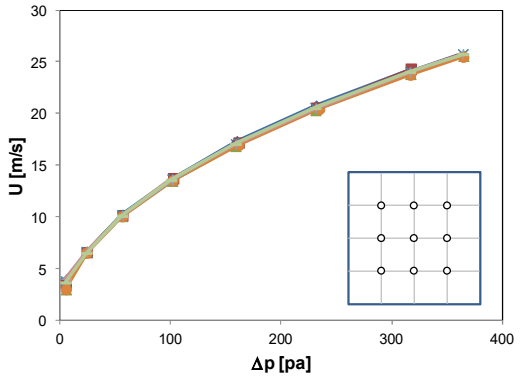

Figure 2. *Measured cross flow velocity distribution with the tunnel contraction pressure drop, over the central nine points marked in the inset plot.*

One of the main flow diagnostic tools consists of eight radial rakes of total pressure probes that are distributed azimuthally at 45° increments within the inlet, where a fan face would nominally be located. The number of pressure probes on each rake alternates azimuthally between ten and eight as shown schematically in Figure 3 (there are also static pressure ports at the surface next to each rake to compute local Mach number). All pressures are measured using a dedicated 96-channel pressure scanner (uncertainty better than 1% of the time-averaged measurement).

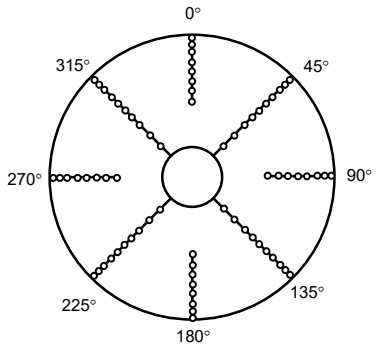

Figure 3. *Azimuthal distribution of the total pressure rakes, alternating between eight and ten probes in each rake.*

Details of the flow topology on the inner surface of the inlet are explored using oil-flow visualization. A mixture of the titanium-dioxide oil paint and linseed oil is iteratively made until its viscosity enables the spreading at the set flow condition. The oil mixture is applied only on the windward side of the nacelle as a continuous thin layer.

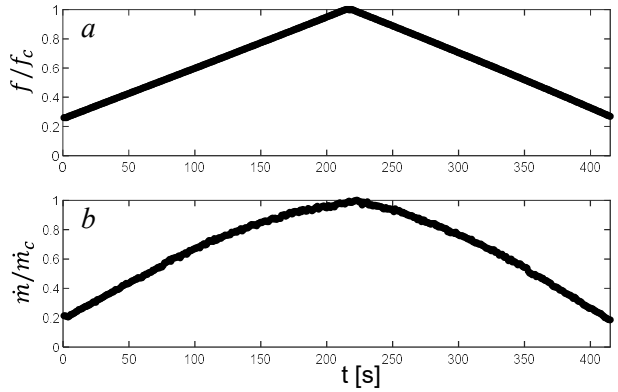

Figure 4. *The commanded ramp-up/down waveform (a) and the corresponding inlet mass flow rate (b).*

The experimental testing procedure is designed to mimic the inlet condition during engine ramp-up/down on a runway, which is illustrated in Figure 4 and efficiently provides a sweep of mass flow rate data for a given crosswind speed and side slip angle. For a given cross flow speed, the operating frequency of the suction blower is monotonically increased at a fixed rate up to the maximum-desired operating point and then monotonically decreased down to the starting operating point at the same rate. The rates of the increase and decrease are low enough to effectively create a quasi-steady variation of the inlet flow (the ramp-up/down commanded signal is shown in Figure 4a). The corresponding change in the actual inlet mass flow rate is directly measured and is shown in Figure 4b for reference. Such simultaneous measurement of the instantaneous inlet flow rates enables the mapping of any recorded flow property to the corresponding time-resolved inlet mass flow rate. To illustrate how the ramp-up/down procedure at sufficiently low rates can reflect any state during the ramp, thirteen operating conditions during the ramp procedure are checked against independent steady operation at each of these conditions. In each of these comparison runs, the inlet mass flow rate is set at each of these thirteen conditions individually, and, following a delay, a set of the total pressure measurements is collected. Figure 5a illustrates the thirteen test conditions with one marked by a solid symbol. For that condition, contour plots of the total pressure are shown in Figures 5b and c, for the time-resolved measurement during ramp-up and during the stationary measurement, respectively. As clearly seen in these two contour plots, both measurements yield indistinguishable total pressure distributions indicating the same flow condition. Similar agreements were achieved for the other twelve operating conditions. It should be noted, however, that some operating combinations of the cross flow speed and the sweep of the inlet mass flow rate result in hysteresis between the ramp-up and ramp-down. Clearly, in such instances, the ramp-down state would be different from the ramp-up state, but this discrepancy would be evident from the measured inlet mass flow rates, as the equivalent plot to Figure 4b would exhibit asymmetry as well.

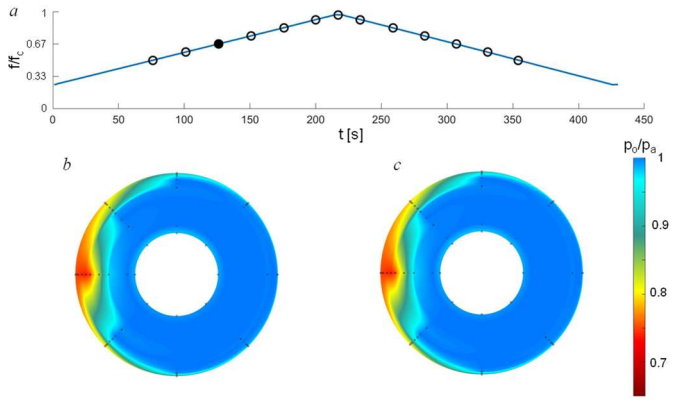

Figure 5. *Operating inlet condition marked by the solid symbol (a) at crosswind speed of 35 knots, characterized by the total pressure contour plot measured during the ramp-up procedure (b) and at-condition (c).*

III. Separation Flow Topology and Flow Control Approach

Nichols et al. (2019) investigated details of the separation topology of the flow drawn into a nacelle inlet in the presence of cross flow. As their analysis showed that the flow bulk flow separation had a signature only across the three windward total rakes, namely those at the azimuthal angles of

225°, 270°, and 315° (cf. Figure 3). These three characteristic normalized total pressure $p^* = (p_o - p_a)/p_a$ profiles are shown in Figure 6 for the cross flow varying between 0 and 40 knots, for a given inlet mass flow rate $\dot{m}^* = 0.99$. The largest total pressure deficit for a fixed crosswind speed occurs at $\theta = 225°$ and 270° for all cases (Figures 6a and b, respectively). The strongest total pressure deficit and its outward extent away from the surface are captured at $\theta = 270°$, while similar trends, albeit to a lesser extent are seen along the lower azimuth at $\theta = 225°$. The deficit at the upper azimuth at $\theta = 315°$ are confined to the surface, indicating no flow separation but rather the outward extended effect of the thickening boundary layer. These results suggest that the azimuthal extent of the separated flow domain does not reach as high as the $\theta = 315°$ azimuth even at the highest cross flow speeds. Each of the total pressure distributions indicate a progressively extending envelope of the total pressure deficit with the cross flow speed, except at the highest azimuth, where much smaller changes are measured within the extending boundary layer.

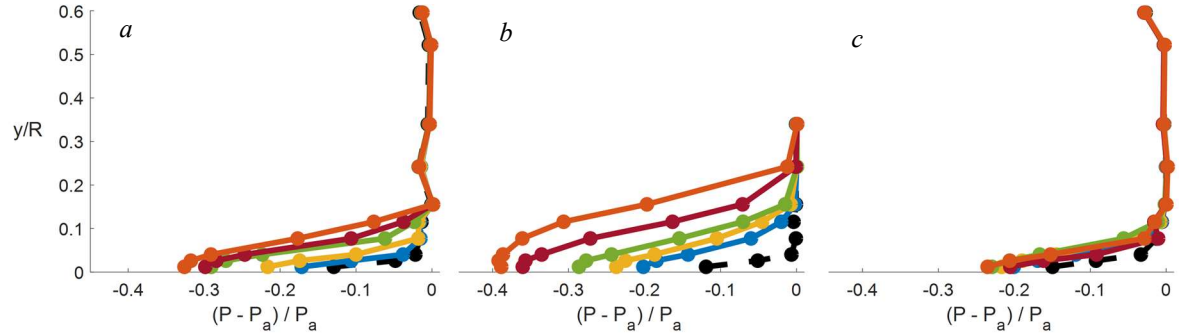

Figure 6. *Normalized total pressure profiles for $\dot{m}^* = 0.99$ at three azimuthal locations $\theta = 225°$ (a), 270° (b), 315° (c) for the cross flow speeds $U_o = 0$ (●), 20 (●), 25 (●), 30 (●), 35 (●), and 40 (●) knots.*

An illustration of the flow separation that is to be addressed by flow control is shown using surface oil-flow visualization of the windward inlet side in Figure 7a for the highest inlet mass flow rate $\dot{m}^* = 0.98$ and cross flow speed of 30 knots. Although the exact separation topology depends on both the inlet mass flow rate and the cross flow speed (Nichols et al, 2019), its main features are typically contained within the azimuthal segment $210° < \theta < 320°$. The main separation domain is typically of a horseshoe pattern that shifts azimuthally, depending on the main flow parameters (in Figure 7a, it is centered at about $\theta = 270°$). The other characteristic feature of the main separation domain is that it is typically bound by two strong recirculating cells, as emphasized in Figure 7a by the two overlaid circulating zones. For cases in which flow separation persists even at the highest flow rates, these circulation cells bounding the separated domain appear to increase in strength with the inlet mass flow rate. Although a single well-defined separation domain remains a signature of the moderate

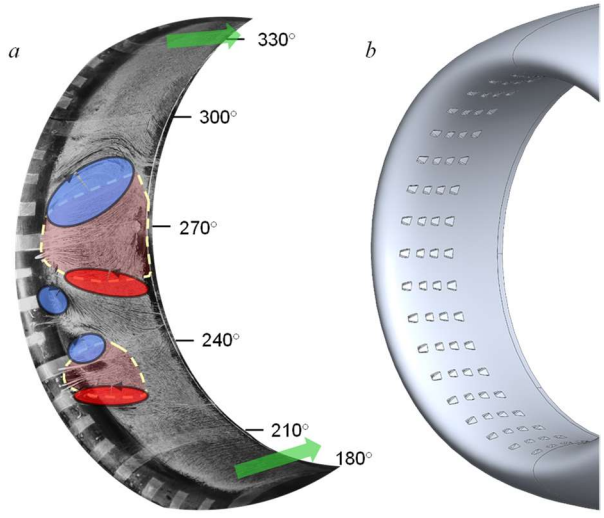

Figure 7. *Flow separation topology on the inlet windward side for $\dot{m}^* = 0.98$ and Uo = 30 knots (a) and the full array of fluidic-oscillating jets distributed over the windward side (b).*

inlet flow rates, the separation flow complexity increases at the highest rates, as evidenced by formation of the secondary separation cells in the case shown in Figure 7a. A small compact secondary separation region that mimics the main one is centered at just below $\theta = 240°$, and it is bound by the circulating cell above and the extended separation cell along its lower boundary. Still, the axial extent of this secondary separated region is limited, and it does not extend to the streamwise positions of total pressure rakes. Just as the secondary separation domain forms on the lower side of the main separation domain through the evolution of multiple small cells, Nichols et al. (2019) showed that another small cell can appear along the inlet lip just below the secondary separated region. Hence, it appears that, with the increase in the inlet flow rate, there is a concomitant azimuthal shift of the main separation region, bound with progressively strengthening circulation cells, while the hierarchy of smaller separation cells open below the preceding ones. Still, they are all typically nested within the azimuthal segment $210° < \theta < 320°$. It should be noted that in either outward direction, the flow relaxes back to its nominal axial direction (in the absence of cross flow), either towards $\theta = 180°$ from above or towards $\theta = 360°$ from below. These features are also emphasized by the directional arrows in Figure 7a.

The base flow assessment summarized in discussion of Figure 7a and presented in more detail by Nichols et al. (2019) points to the two main requirements for the flow control strategy aimed at alleviating the detrimental effects of the inlet flow separation. First, it is expected that, regardless of the particular set of the flow parameters (inlet mass flow rate and the cross flow speed), the region that needs to be addressed would be azimuthally bound within approximately $210° < \theta < 320°$. Second, and more importantly, as the flow separation topology changes within this segment with the flow parameters, it is expected that the optimal flow control would need to adapt to the changing flow conditions. To test this flow control strategy based on the understanding of the base flow evolution, a prototype flow control inlet is designed and manufactured. It is primarily designed for the screening purposes of a number of the flow control configurations, which required a wide coverage of the windward inner surface of the inlet. The windward surface of the control inlet model is shown in Figure 7b, where axial arrays of four flow control jets are distributed azimuthally over the windward azimuthal half. Although the available jets spread past the estimated azimuthal range of $210° < \theta < 320°$, it will be shown that there is no need to utilize any of them that lie outside of the flow separation bounds. The actual configuration of any subset of the available control jets is done internally within the model. This control model design therefore enabled easy reconfiguration and testing of many flow control configurations with a single inlet model. While Nichols et al. (2019) initially tested applicability of autonomous bleed as the flow control elements, the present work explores utilization of the fluidic oscillating jets developed over years at Georgia Tech and already used in many internal and external flow control applications (e.g., Vukasinovic et al., 2013, Burrows et al., 2019). More details about this type of the fluidic oscillating jet operation can also be found in the work by Gregory et al. (2007) and Raghu (2013). This type of actuator transforms a steady fluid dual stream into a self-oscillating jet solely based on the actuator internal geometry that gives a rise

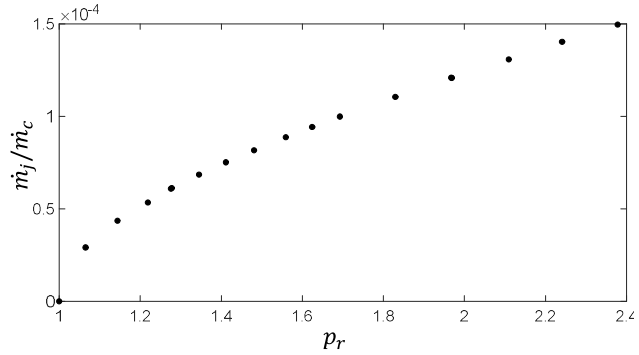

Figure 8. *Fluidic-oscillating jet mass flow rate with the pressure ratio.*

to the fluidic instability. A particular advantage of this actuator is the absence of any moving parts. This type of fluidic oscillator thus combines both the steady component of the added mass flow rate to the flow with the unsteady effects that typically enhance its performance via increased mixing when compared to the steady jets.

Prior to utilization of these flow control elements, they are also tested on a bench, primarily relating the supply pressure, i.e., the pressure ratio across the actuator, with its output in terms of the jet mass flow rate, which is presented in Figure 8. Aside from a steep rise at the pressure ratios just above 1, there is a rather proportional relationship between the fluidic oscillating jet output at its supply pressure.

IV. The Effects of Crosswind on Inlet Distortion

The presence of crosswind effects the inlet flow detrimentally, increasing both the intake losses and, even more importantly, the total pressure distortion of the flow passing the fan blades. To illustrate the induced total pressure deficit and its distribution at the fan face, Figure 9 shows the characteristic total pressure contour plots for the three inlet mass flow rates $\dot{m}/\dot{m}_c$ = 0.3, 0.6, and 0.9 at the two cross flow speeds of interest – 30 and 35 knots. As a reference, equivalent contour plots are shown also in the absence of cross flow. First, base flows in the absence of the crosswind (Figures 9a–c) indicate almost no total pressure deficit, besides very small nonuniformities near the wall at the highest mass flow rate. This is clearly expected as the outer air gets smoothly drawn into the inlet under this nominal condition. A quite different scenario is seen in the presence of the U_o = 30 knots crosswind (Figures 9d–f). Due to the flow separation on the windward side, there is a rather centered total pressure deficit at any of the lower two flow rates which begins to skew downward at the highest flow rate. Besides the increase in the deficit with the mass flow rate, it is also notable that its distribution changes at the highest flow rate (Figure 9f), as the deficit spreads azimuthally, but also becomes confined closer to the surface. A similar trend is seen in the presence of the U_o = 35 knots crosswind (Figures 9g–i). At the lowest intake speed (Figure 9g), the distortion is nearly identical to the 30 knot case (Figure 9d) besides a slightly larger azimuthal spreading on the lower half of the inlet. As the flow rate increases (Figure 9h-i), the total radial extent of the distortion remains nearly constant to the equivalent 30 knot case (Figure 9e-f), with the main difference being the intensity of the distortion in this region. As evidenced by the larger region of higher distortion predominately at 270°, the separation at this

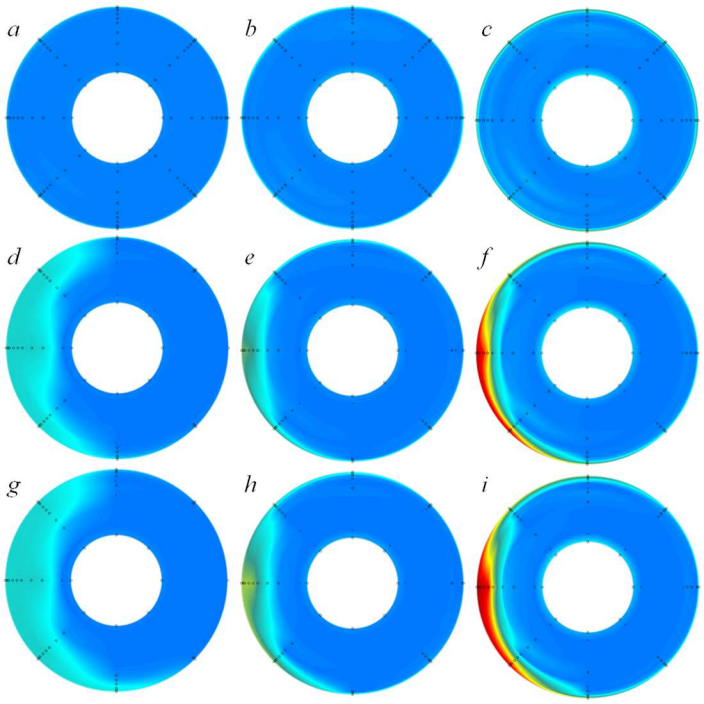

Figure 9. *Base flow total pressure contour plots for the cross flow speeds U_o = 0 (a–c), 30 (d–f), and 35 (g–i) knots and the inlet normalized mass flow rates of $\dot{m}^*$ = 0.3 (a,d,g), 0.6 (b,e,h), and 0.9 (c,f,i).*

area is stronger and produces a larger effect on the flow field. There is evidence of additional azimuthal spreading of the distortion to the lower half of the inlet in these cases as well.

There are many parameters that characterize a total pressure distortion relevant to the airplane engine. The one adopted in the present work is the circumferential distortion index, *IDC* (see Colin et al., 2007) which characterizes the circumferential heterogeneity of the total pressure distributions over the fixed radii, by examining the departures between each averaged total pressure and the minimum one along the full turn at the radius. Finally, the maximum *IDC* index over all of the considered radii for any given condition yields the maximum distortion parameter $IDC_{\max}$ that is used as the main assessing parameter. To establish the reference base for the flow distortion in the presence and absence of the cross flow, the initial assessment of the $IDC_{\max}$ distribution is done for the default inlet geometry, without any of the flow control elements integrated into its moldline. Figure 10 shows the extracted distributions of the $IDC_{\max}$ parameter for the absence and presence of the cross flow of 30 and 35 knots, as measured during the described ramp-up/down procedure (cf. Figure 4) using the blower sweep procedure described in Section II. In the absence of the cross flow, all the total pressure deficit is compressed close to the surface, as the only source of the deficit is confined to the boundary layer. Although the overall levels of $IDC_{\max}$ are rather low, there is still a consistent increase with the inlet mass flow rate due to the corresponding increased losses. Still, the maximum coefficient levels seem to be centered about 0.05, or 5%. It also appears that there is several-percent scatter of the $IDC_{\max}$ at these highest levels, which may point to the higher flow overall unsteadiness about the maximum inlet flow rates. There is a rather dramatic change in the $IDC_{\max}$ distribution in the presence of cross flow speeds that induce flow separation over the inlet's windward side, which is reflected in considerably elevated levels of the $IDC_{\max}$ index for both the cross flow speeds shown in Figure 10. These measured distortions are predominantly affected by the local flow separation, which clearly induces significant inhomogeneity along the circumferential direction, as a large portion of the inlet flow is not significantly affected by the cross flow presence. There is an offset in $IDC_{\max}$ even at the lowest inlet flow rates and the slope of the $IDC_{\max}$ increase rises with the cross flow speed, such that the peak values of about 0.23 and 0.26 are reached for the maximum flow rates at U_o = 30 and 35 knots, respectively.

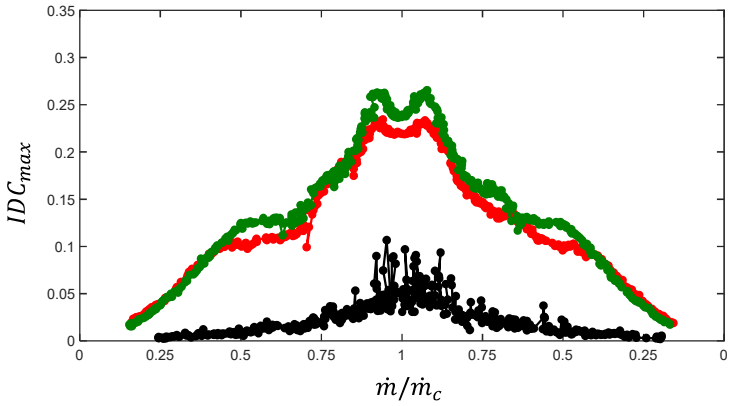

Figure 10. *Distortion index IDCmax distribution with the inlet mass flow rate for the default inlet geometry at cross flow speeds U_o = 0 (●), 30 (●), and 35 (●) knots.*

So that multiple flow control configurations can be screened using a single inlet, a large number of jet orifices modify the inner inlet surface, as seen in Figure 7b. Any optimized flow control configuration would require substantially fewer active jets, and therefore much lesser modifications of the inlet surface. The present impact of the (inactive) jet orifices on the total pressure distortion is presented in Figure 11 in the absence and presence of the cross flow of U_o = 30 and 35 knots. Overall, it is seen that the modified inlet moldline that accommodates the flow control jets does not significantly alter the $IDC_{\max}$ distribution across the full mass flow rate sweep procedure, even in the presence of cross flow. This is particularly true in the absence of

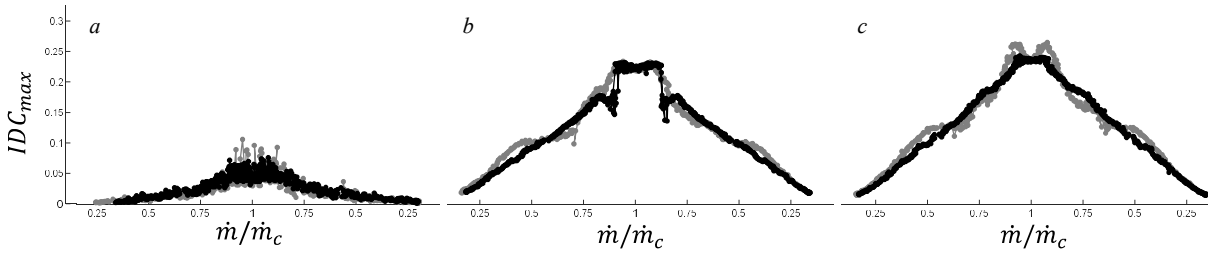

Figure 11. *Distributions of the distortion parameter IDC_{max} with the inlet mass flow rate for the default smooth (●) and inactive flow control inlet (●) for cross flow speeds of U_o = 0 (a), 30 (b), and 35 (c) knots.*

cross flow (Figure 11a) where the same central magnitudes of the distortion index are measured. It appears that the inactive jet orifices possibly even tripped the boundary layer flow such that the high excursions of the $IDC_{\max}$ at the highest inlet flow rates are suppressed. Similar results are exhibited for the IDC_{max} distributions in the presence of crosswinds of 30 (Figure 11b) and 35 (Figure 11c) knots, as the initial rise of the $IDC_{\max}$ during the ramp-up procedure persists at the unchanged slope for the flow control module, while the 'smooth' inlet behavior changes slope at $\dot{m}^*$ = 0.4 and 0.7 for the lower cross flow speed (Figure 11b) and at about $\dot{m}^*$ = 0.5, 0.8, and 0.9 for the higher cross flow speed (Figure 11c). The only departure from the smooth changes in the distortion parameter with the inlet mass flow rate is seen between $\dot{m}^*$ = 0.8 and 0.9 for U_o = 30 knots, where the initial drop in the $IDC_{\max}$ is followed by the steep rise to its maximum level. Such discontinuous changes in the $IDC_{\max}$ parameter are typically related to the sudden formation of additional azimuthal separation cells, or a possible switching between different azimuthal regions of the flow separation. Each of these precipitates the emergence of an altered flow separation topology, which was discussed in more detail by Nichols et al. (2019). The second notable difference is seen about the highest levels of the inlet mass flow rate for U_o = 35 knots (Figure 11c), where the $IDC_{\max}$ of the smooth inlet surface exhibits a small tip towards $\dot{m}^*$ = 1, while that of the flow control inlet remains at a steady level. Nonetheless, $IDC_{\max}$ levels are practically identical for the highest inlet mass flow rate ($\dot{m}^*$ = 1) in all the three cases depicted in Figure 11.

V. Active Flow Control

Following the findings by Nichols et al. (2019) of the inlet flow separation topology change with the inlet mass flow rate (for a given cross flow speed), it is decided to consider three characteristic flow regimes, marked by the low, mid, and high inlet flow rates, where $\dot{m}^*$ = 0.3, 0.6, and 0.9 are selected, respectively.

First, the cross flow speed of U_o = 30 knots is investigated by assessing these three characteristic separation topologies. For that purpose, surface oil-flow visualization is conducted on the flow control inlet, in a similar manner done before on the default inlet model with the smooth inner surface. Figure 12 shows the resulting traces of the oil flow visualization over the windward inner surface of the flow control inlet. The jet orifices are present on the surface but are inactive for this set of visualizations. Particular interest is placed on isolating the separated flow domains for each of the three cases, with the separation bounds emphasized by the overlaid dashed curves. Each of the separated domains progressively widen azimuthally with increased axial distance into the inlet, forming a horseshoe-like pattern. The formation of the separation past the inlet lip at the lowest inlet mass flow rate (Figure 12a) is skewed towards the lower azimuthal angles (relative to the central horizontal plane), forming at about θ = 225° and remaining open up to about θ = 285°. As the separation widens in the axial direction, its extent spreads approximately over

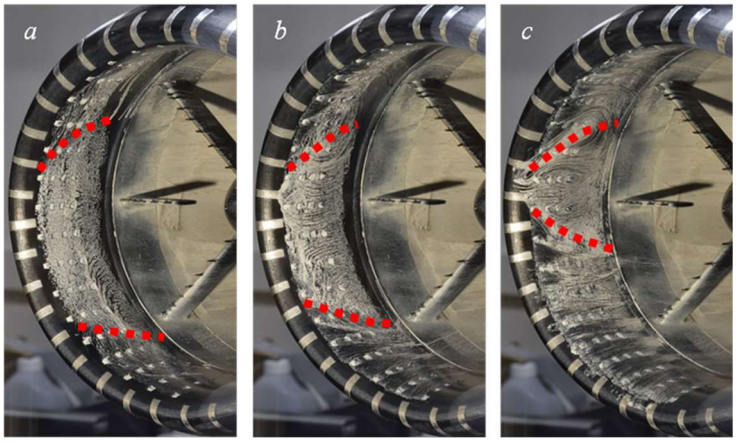

Figure 12. *Surface oil-flow visualization of the windward inlet inner surface for U_o = 30 knots and m/m_c = 0.3 (a), 0.6 (b), and 0.9 (c). Separated domain bounds are marked by the dashed lines.*

$210° < \theta < 305°$ just before the total pressure rakes. Although the separation domain is skewed downward, it should be noted that there is a strong angularity of the flow outside of the upper separation boundary, at higher values of θ. As previously discussed in all of the other cases that were characterized by the surface oil-flow visualization, the flow outside of the separated domain progressively relaxes back to purely axial intake flow in the proximity of the bottom and top orientations, e.g., towards θ = 180° and 360°, respectively. Lastly, at this low inlet flow rate, there is no clear imprint of the circulating cells that typically bound the separated domain. The main change in the separation topology that is observed at the moderate inlet mass flow rate case (Figure 12b) is the azimuthal shrinking of the separation domain, which mostly retreats 'from below', as the upstream separation point does not separate up to about θ = 235°, while the upper end of the flow separation barely shifts upward. The other notable change is that the typical circulating cells at the bounds of the separated flow are clearly visible at this flow rate, contrary to the lowest mass flow rate case. Finally, a rather dramatic shift in the separated region is seen at the highest flow rate (Figure 12c), where the separated domain lower bound shifts considerably upward, and the separation domain opens at just about θ = 270°. The upper bound still does not move significantly, resulting in the separated region being centered above the horizontal central plane. Another trend observed for the previous case is continued–the recirculating cells that bound the separated domain appear to continue growing in size and strength with this further increase in the inlet mass flow rate. Also, as pointed in discussion of the highest inlet mass flow rate discussed in Figure 7a, small secondary circulation cells begin to form on the inlet inner lip, just below the lower bound of the main separation domain.

Analysis of the separation flow topology discussed in connection to Figure 12, guided the selection of the flow control configurations that are optimized for mitigation of the three characteristic separation patterns for $\dot{m}^*$ = 0.3, 0.6, and 0.9. Regardless of the particular inlet mass flow rate, each flow control configuration begins at the most upstream location that matches the incipient flow separation, and its azimuthal extent approximately matches the azimuthal extent of the flow separation. It is found that a slight extension of the flow control coverage into the strongly angular, but not necessarily separated flow at higher θ is beneficial. The total extent for the $\dot{m}^* = 0.3$ case (Figure 13a) is $210° < \theta < 320°$, while for $\dot{m}^* = 0.6$ is $240° < \theta < 320°$ (Figure 13b), and for the highest mass flow rate, it is reduced to $240° < \theta < 300°$. The number of active jet columns is determined by their relative contribution, and the two cases with the lower mass flow rates utilize the first two columns, as the added benefit of any subsequent active jet column has diminishing returns. Reconfiguration of the flow control pattern for the highest inlet mass flow rate (Figure 13c) is driven by the strong circulating cells that are characteristic for this case. It is found (not shown here for brevity) that even the use of only the first two columns of active jets results in the

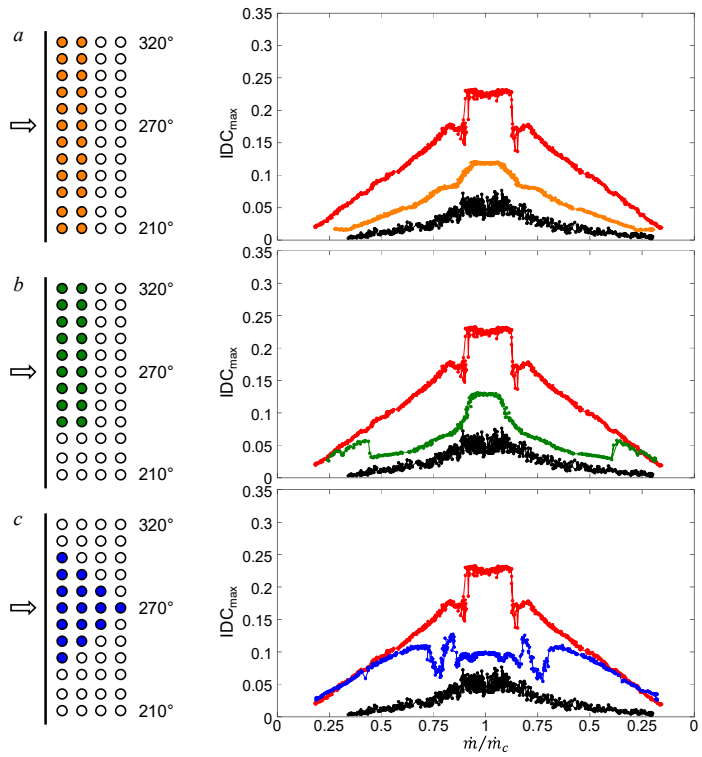

Figure 13. *Flow control configuration and the resulting distributions of the uncontrolled (red) and controlled (color) distortion index IDC_{max} with $\dot{m}/\dot{m}_c$ for U_o = 30 knots and the flow control optimized for the low (a), mid (b), and the high (c) inlet mass flow rates. IDC_{max} distribution in the absence of cross flow is shown in black for reference.*

substantial flow control effect, but extension into the shown triangular patter enables further notable improvement, especially at the highest inlet flow rates.

Although the three proposed flow control configurations target specific extents of the inlet mass flow rates, each of them is tested throughout the full range of the mass flow rates and at the fixed flow control parameter C_q = 0.27% (a ratio of the total jet mass flow rate to the max inlet mass flow rate), according to the outlined ramp-up/down procedure of Figure 4. Figure 13a shows the resulting distribution of the IDC_{max} distortion index at U_o = 30 knots in the absence of flow control (in red) and for the flow control tailored for the lower inlet mass flow rates (in orange). The reference distortion parameter distribution is plotted in black in the absence of cross flow. Although the flow control is predominantly tailored for the lowest inlet flow rates, it is seen that it has a substantial broadband effect in the distortion reduction over the full range of the inlet flow rates. It is capable of suppressing the distortion parameter from approximately 5% to sub-2% at $\dot{m}^* = 0.3$, and maintaining a very low distortion levels even up to $\dot{m}^* = 0.6$. This particular flow configuration is capable of lowering the distortion from about 23% in the uncontrolled flow to about 12% in the controlled flow at the highest inlet mass flow rate–a reduction of nearly 50%. It is also noted that the smallest effect of this flow control scheme is seen at the highest mass flow rates, between $\dot{m}^* = 0.8 - 1$, where the IDC_{max} slope sharply increases. Results for the distortion change with the flow control configuration designed for the mid-range of the inlet mass flow rates are shown in Figure 13b. As this flow control configuration is designed for the

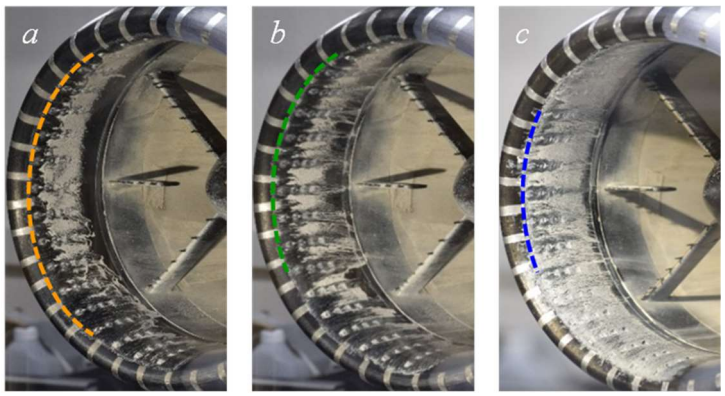

Figure 14. *Surface oil-flow visualization of the windward inlet inner surface for U_o = 30 knots and $\dot{m}/\dot{m}_c$ = 0.3 (a), 0.6 (b), and 0.9 (c), controlled by $C_q \approx 0.27\%$. Azimuthal extent of the active jets is marked by the dashed lines.*

mid-range flow rates, its initial effectiveness at the very low flow rates is only marginal, as the controlled IDC_{max} is only slightly below the uncontrolled values. However, once the mid-range flow rates are attained, at about $\dot{m}^* = 0.4$, a sharp drop in the IDC_{max} marks the flow attachment due to the flow control, and the low levels of distortion are maintained thereafter up to about $\dot{m}^* = 0.7$. However, a rather sharp drop off in performance is seen at the approach of the highest flow rates, even so that this configuration performs worse at the highest $\dot{m}^*$ than the one designed for the lowest flow rates, but still delivering a substantial 40% reduction compared to the uncontrolled case. Finally, the effect of the flow control designed for the highest inlet flow rates is shown in Figure 13c. Not surprisingly, its effect is very weak all the way to about $\dot{m}^* = 0.6$, where shortly after it is shown to attach the separated flow, marked by the sharp drop in the IDC_{max}, only to quickly reseparate, followed by another reattachment at about $\dot{m}^* = 0.85$, and keeping the flow attached thereafter. Consequently, this flow control configuration performs the best within the region of intended design, reducing the IDC_{max} by almost 60%.

The resulting controlled flow topology at U_o = 30 knots and the three characteristic flow control configurations designed for the three inlet flow rates is visualized by the surface oil flow, just as in the absence of the flow control shown in Figure 12. The windward inner surface visualizations are shown in Figure 14, where the azimuthal extent of the active flow control jets is marked by the dashed lines. A common feature of all of the controlled flow topologies is that the dominant flow separation domain is suppressed in each of the controlled cases, which clearly illustrates why the index of the total distortion measure was dramatically reduced at each of the targeted inlet mass flow rates.

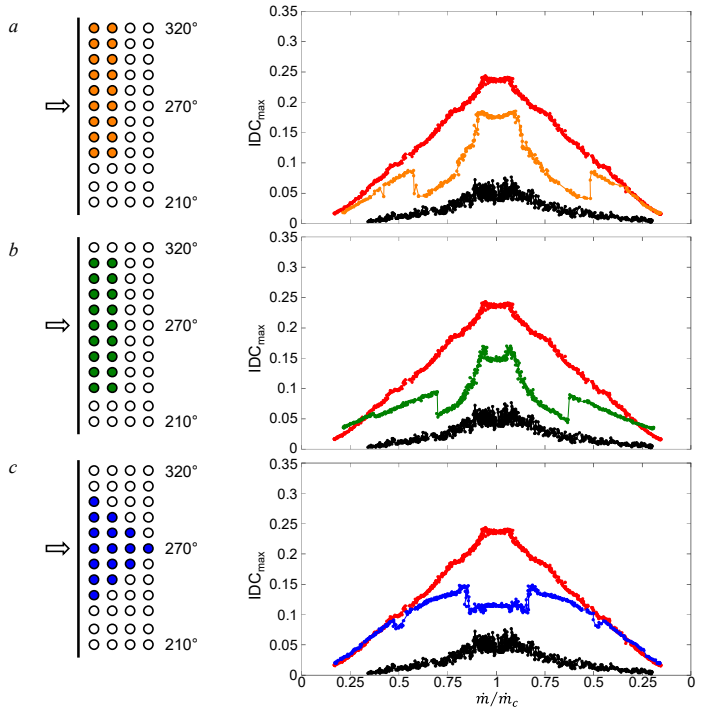

Figure 15. *Flow control configuration and the resulting distributions of the uncontrolled (red) and controlled (color) distortion index IDC_{max} with $\dot{m}/\dot{m}_c$ for U_o = 35 knots and the flow control optimized for the low (a), mid (b), and the high (c) inlet mass flow rates. IDC_{max} distribution in the absence of cross flow is shown in black for reference.*

The same investigation is conducted for the highest cross flow speed of 35 knots. The oil flow visualization (not shown) guided the three flow control configurations targeting the low, mid, and high flow rate domains of the inlet operation. It is found that, similar to the case of 30 knots cross flow, iterative flow control configurations need to be applied, each of which is schematically shown in Figure 15. Furthermore, each of the flow control configurations utilized the same flow control coefficient C_q = 0.27%, just as in the lower cross flow case. The resulting effects on the distortion index IDC_{max} over the full range during the ramp-up/down procedure are shown in Figure 15. Although there is a broadband reduction in distortion in each of the considered configurations, it is notable that the

overall effect of the flow control is reduced relative to the previous cases for U_o = 30 knots. A dramatic drop off in the distortion for the flow control configuration designed for the lowest inlet flow rates (Figure 15a) is seen only past $\dot{m}^* = 0.55$, while the mid-range control successfully attached the separated flow past about $\dot{m}^* = 0.7$, marked by the sharp drop in distortion in either case. The flow control configuration designed for the highest inlet flow rates (Figure 15c) in nonetheless capable of significant reduction in the distortion parameters about $\dot{m}^* = 1$, reducing the uncontrolled levels of $IDC_{\max}$ by about 50% at this range of the most importance.

The results presented above clearly indicate that the proposed flow control reconfiguration relative to the changing flow topology can indeed optimize the flow control effectiveness based on its metrics (in the present case – the circumferential distortion parameter $IDC_{\max}$) over the full envelope of the inlet/engine mass flow rates. To illustrate a potential of reconfiguring the flow control jets in real time, this is *conceptually* done in Figure 16 based on the segment-optimized flow control over the three characteristic flow regimes at 30 and 35 knots cross flows. Here, the three segmented flow control configuration results (in terms of the $IDC_{\max}$ distortion index) are combined into a possible sequence of switching between the segmented optimal configuration with the continuous ramp up/down of the inlet mass flow rate for the cross flow speed of 30 (Figure 16a) and 35 (Figure 16b) knots. Clearly, as the inlet mass flow rate is ramped up, initial flow control is assumed to be done by the flow control configurations designed for the lowest inlet flow rates, where its activation is marked by an arrow. As the inlet mass flow rate continues to increase, at some point the mid-range designed flow control begins to perform better than the initial flow control configuration, and a notional switch to this flow control configuration is again marked by another arrow. Finally, as the inlet mass flow rate approaches the highest levels and the effectiveness of the mid-range control begins to drop, the final notional switch is made to the flow control configuration that is optimized for this range of the inlet flow rates. This final switch point is also marked by an arrow. Clearly, once the inlet flow rate begins to ramp down, this whole notional switch procedure is repeated in the reversed order – the high flow rate flow control is kept until the inlet flow rate drops sufficiently for the mid-range flow control to outperform the high flow rate one. Similarly, as the inlet mass flow rate continues to decrease, eventually it drops below the threshold for the flow control at the lowest flow control configuration, when the final notional switch is made. Each of the plots in Figure 16 has the $IDC_{\max}$ distribution for the same inlet mass flow rate sweep in the absence of crosswind (in black), which serves as the absolute lower bound of detrimental effect that the cross flow introduces (in red). The ultimate performance of the flow

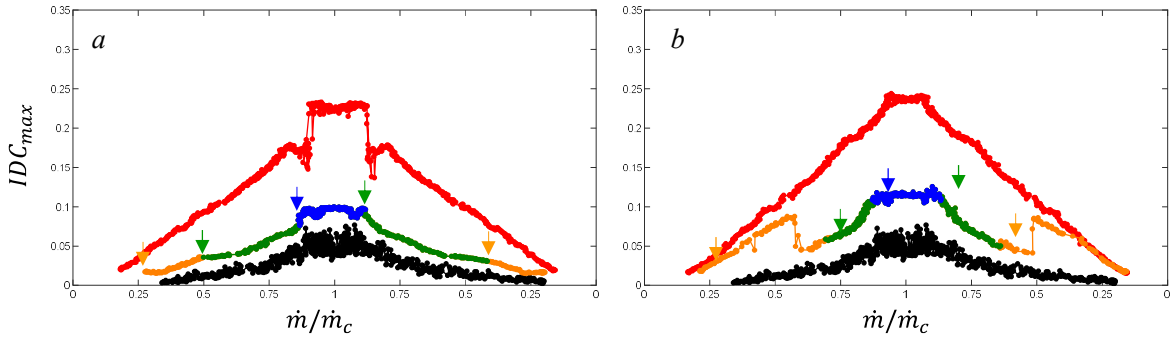

Figure 16. *Conceptual switching between the three locally-optimized flow control configurations of Fig. 15 for the broad $\dot{m}/\dot{m}_c$ optimized reduction of the IDCmax distortion index for U_o = 30 (a) and 35 (b) knots. All color representations are kept the same as in Fig. 15.*

control would convert the inlet flow state with the presence of cross flow back to its performance in the absence of it. It is seen that the notional flow control switching exercise done in Figure 16 suggests that there is a reasonable expectation that the real-time flow control reconfiguration would be capable of reverting the 30 knots cross flow case (Figure 16a) very close to the inlet performance in the absence of the cross flow. Somewhat lesser, although still significant combined effect is seen for the cross flow speed of 35 knots (Figure 16b). Lastly, it should be noted that both of these cross flow speeds were controlled using the same total jet mass flow rate coefficient $C_q = 0.27\%$ for each configuration. It is argued that both of these flow control approaches, and particularly that of the higher cross flow speed, would benefit from the somewhat increased flow control parameter C_q, i.e., that the optimal C_q for the best flow control effect would be dependent of the cross flow speed.

VI. Conclusions

The present experimental investigation builds on the earlier work of Nichols et al. (2019) who explored the complex topology of flow separation over the windward inner surface of an engine nacelle inlet in the presence of cross flow. Of particular interest in the present investigations are the changes in flow separation patterns with variations in the cross and inlet flows which are used to guide spatial configurations of fluidic actuation for optimal mitigation of global distortion effects.

The present investigations are conducted in a nacelle cross flow facility in which a nacelle model operating in suction is placed in a crosswind wind tunnel such that its attitude relative to the oncoming flow is adjustable. The test conditions are designed to mimic engine ramp up and down by varying the inlet mass flow rate at a given (preset) crosswind speed. While multiple crosswind speeds have been tested, the present study focuses primarily on cross flow speeds for which massive azimuthal separation cells were observed by Nichols et al. (2019) namely, 30 and 35 knots. The selection of the flow control configurations was motivated by two important observations. First, although the spatial extent and azimuthal orientation of the separation domain would change, its azimuthal range is typically nested within the domain $210° < \theta < 320°$ (over the windward inner surface where $\theta = 270°$ is pointing towards the oncoming cross flow). This range determined the overall azimuthal extent of the surface arrays of flow control actuators. Second, and perhaps more important, the changes in the topology of the separation for changing flow rate underscored the need for corresponding spatially-adjustable flow control configurations.

Spatially-variable actuation configurations are investigated by segmenting the range of inlet flow rate into three characteristic, partially-overlapping domains centered about $\dot{m}^* = 0.3$, 0.6, and 0.9, and the actuation was configured based on the dominant features of the separation cells in each domain. This was accomplished using arrays of individually-addressable fluidic oscillating jets integrated on the inner surface of the nacelle model. It is shown that the control configuration for each inlet mass flow rate domain leads to significant mitigation of the total pressure distortion as measured by the circumferential distortion index IDC_{max}. It is also noted that these effects extend well beyond the range of each of the domains. When considering the optimal performance for each inlet mass flow rate domain, the overall reductions in IDC_{max} were up to 60% and 50% at 30 and 35 knots crosswind, respectively. The control input utilized for such effectiveness is measured by the fraction of the total actuation mass flow rate relative to the maximum inlet mass flow rate, which is less than 0.3%.

The successful implementation of segment-optimized spatial flow control configurations indicates that dynamic, real-time reconfiguration of the fluidic actuation with varying inlet- and crosswind conditions could yield an optimal control of inlet separation during takeoff/landing and taxiing.

Acknowledgment

This research has been supported by The Boeing Company, Georgia Tech, and the National Science Foundation Graduate Research Fellowship under Grant No. DGE-1650044.

References

Burrows, T.J., Vukasinovic, B., Lakebrink, M.T., Mani, M., and Glezer A. Control of Flow Distortion in Offset Diffusers using Trapped Vorticity, Int. J. Heat Fluid Fl. 75, pp. 122-134, 2019.

Colehour, J.L., and Farquhar, B.W., "Inlet Vortex," *J. Aircr.*, vol. 8, no. 1, pp. 39–43, 1971.

Colin, Y., Aupoix, B., Boussuge, J.F., and Chanez, P., "Numerical Simulation and Analysis of Crosswind Inlet Flows at Low Mach Numbers," *Proc. 8th Int. Symp. Exp. Comput. Aerothermodyn. Intern. Flows*, 2007.

Gregory, J. W., Sullivan, J. P., Raman, G., and Raghu, S. "Characterization of the microfluidic oscillator," AIAA Journal, 45, 2007, pp. 568–576.

Hall, C.A., and Hynes, T.P., "Measurements of Intake Separation Hysteresis in a Model Fan and Nacelle Rig," *J. Propuls. Power*, vol. 22, no. 4, pp. 872–879, 2006.

Maji, F., Efraimsson, G., and Reilly, C. J. O., "Potential Improvement of Aerodynamic Performance by Morphing the Nacelle Inlet," *Aerosp. Sci. Technol.*, 54, 122–131, 2016.

Nichols, D.A., Vukasinovic, B., Glezer, A., DeFore, M.C., Rafferty, B. and Palacios, F.D., "Characterization and Control of Nacelle Inlet Flow in Crosswind," *AIAA Aviation 2019*, AIAA Paper 2019-3685.

Radespiel, R., François, D.G., Hoppmann, D., Klein, S., and Scholz, P., "Simulation of Wing and Nacelle Stall," *AIAA SciTech*, AIAA Paper 2016-1830.

Raghu, S., "Fluidic oscillators for flow control," Experiments in Fluids, 54, 2013, 1455.

Savelyev, A.A., Mikhaylov, S.V., and Zlenko, N.A., "Aerodynamic Inlet Design for Civil Aircraft Nacelle," *Proc. 29th Congr. Int. Counc. Aeronaut. Sci.*, 2014.

Trapp, L.G., and Girardi, R., "Evaluation of Engine Inlet Vortices Using CFD," *50th AIAA Aerosp. Sci. Meet. Incl. New Horizons Forum Aerosp. Expo.*, AIAA Paper 2012-1200.

Trapp, L.G., Argentieri, H.G., de Souza, F.J., and Girardi, R.M., "Aspects of Isolated Nacelles Near the Ground During Crosswind Operation," *Proc. ENCIT 2006*, 2006.

Übelacker, S., Hain, R., and Kähler, C.J., "Flow Investigations in a Stalling Nacelle Inlet Under Disturbed Inflow," *Adv. Simul. Wing Nacelle Stall.*, vol. 131, pp. 271-283, 2016.

Übelacker, S., Hain, R., and Kähler, C.J., "Flow Investigations in a Stalling Nacelle Inlet," *Proc. 17th Int. Symp. Appl. Laser Tech. to Fluid Mech.,* 2014.

Vukasinovic, B., Glezer, A., Gordeyev, S., Jumper, E., and Bower, W. W., Flow Control for Aero-Optics Application, Exp. Fluids 50:1492, 2013.

Wakelam, C.T., Hynes, T.P., Hodson, H.P., Evans, S.W., and Chanez, P., "Separation Control for Aeroengine Intakes, Part 1: Low-Speed Investigation of Control Strategies," *J. Propuls. Power*, vol. 28, no. 4, pp. 758–765, 2012a.

Wakelam, C.T., Hynes, T.P., Hodson, H.P., Evans, S.W., and Chanez, P., "Separation Control for Aeroengine Intakes, Part 2: High-Speed Investigations," *J. Propuls. Power*, vol. 28, no. 4, pp. 766–772, 2012b.